

Numerical study of liquid metal flow in a rectangular duct under the influence of a heterogenous magnetic field

Evgeny V. Votyakov¹, Egbert A. Zienicke

Abstract: We simulated numerically the laminar flow in the geometry and the magnetic field of the experimental channel used in [Andreev, Kolesnikov, and Thess (2006)]. This provides detailed information about the electric potential distribution for the laminar regime (numerical simulation) and in the turbulent regime as well (experiment). As follows from comparison of simulated and experimental results, the flow under the magnet is determined by the interaction parameter $N = Ha^2/Re$ representing the ratio between magnetic force, determined by the Hartmann number Ha , and inertial force, determined by the Reynolds number Re . We compared two variants: (i) $(Re, N) = (2000, 18.6)$ (experiment), $(400, 20.25)$ (simulation), and (ii) $(Re, N) = (4000, 9.3)$ (experiment), $(400, 9)$ (simulation) and found an excellent agreement for the numerical and experimental distributions of the electric potential. This is true despite of the fact that the experimental inflow is turbulent while that in the simulation is laminar. As a special feature of the electric potential distribution local extrema under the magnets are observed, as well experimentally as numerically. They are shown to vanish, if the interaction parameter falls below a critical value. Another interesting new detail found in our numerical calculations is the appearance of helical paths of the electric current. Using a simplified magnetic field without span-wise dependence, we show that important physical features of the considered problem are sensitive to small variations in the spatial structure of the magnetic field: the local extrema of the electric potential and also the helical current paths disappear when the simplified magnetic field is used. The structure of the three dimensional velocity field is also investigated, in particular, a swirling flow is found in the corners of the duct caused by Hartmann layer destruction behind the magnets.

keyword: 3D Numerical simulation, laminar liquid

metal flow in a rectangular duct, localized heterogenous magnetic field

1 Introduction

The flow of an electrically conducting fluid under a localized inhomogeneous magnetic field is of interest for many industrial applications dealing with the problem to influence hot metal melts by the use of magnetic fields. This has the advantage that no direct contact with the chemically aggressive melt is necessary [Davidson (1999)]. One prominent example is the electromagnetic brake used in modern continuous steel casting, see for instance [Takeuchi, Kubota, Miki, Okuda, and Shiroyama (2003)]. If one neglects the liquid steel jets entering the mould, the flow in a liquid metal channel under a static localized magnetic field may reproduce qualitatively many features of the electromagnetic brake: the braking effect on stream-wise velocity, suppression of turbulence under the magnet, and effects of strong spatial dependence of the magnetic field. Another example, where liquid metal flow in a channel is important for possible industrial applications, is the Lorentz Force Velocimetry based on exposing the fluid to a magnetic field and measuring the drag force acting upon the magnetic field lines [Thess, Votyakov, and Kolesnikov (2006)].

In the recently appeared experimental work [Andreev, Kolesnikov, and Thess (2006)] the liquid metal flow was systematically investigated for the range of interaction parameters $4 \leq N \leq 20$. In the experiments special attention was focused on the suppression of turbulence by the magnetic field and on a systematic recording of data for the electric potential building up under and around the magnets. As a result, the full map of the electric potential distribution was obtained for the middle horizontal plane of the rectangular duct and few N parameters. If the transverse magnetic field would be homogenous the electric potential data might be used to determine the velocity components perpendicular to the magnetic field [Sommeria and Moreau (1982)]. In the

¹Institut für Physik, Technische Universität Ilmenau, PF 100565, 98684 Ilmenau, Germany

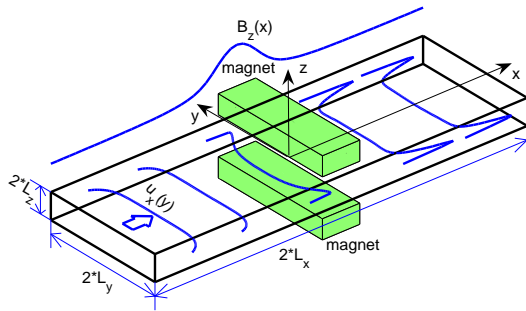


Figure 1: Coordinate system and sketch of the problem: rectangular channel $2L_x \times 2L_y \times 2L_z$ and two magnets on the bottom and top walls. Qualitatively, there are shown transverse magnetic field $B_z(x)$ varying along stream-wise direction, and span-wise profile of stream-wise velocity $u_x(y)$. The center of the coordinate system is in the center of the magnetic gap.

present case of strongly inhomogeneous magnetic field, the electric potential data can be solely compared with the results of the corresponding numerical simulations.

Fig. 1 presents schematically the geometry and magnetic field configuration studied in [Andreev, Kolesnikov, and Thess (2006)]: the liquid metal moves in a rectangular duct, where the locally heterogeneous magnetic field is created by two permanent magnets on the top and bottom walls of the duct. The originally convex velocity profile $u_y(x)$ adopts, by passing the magnetic field $B_z(x)$, a characteristic M shape what is a manifestation of the electromagnetic brake process.

The main goal behind our numerical investigation is first to reproduce features of the flow and the electromagnetic quantities found in the experiment. Moreover, since numerical calculations have the advantage that all quantities are available in the whole computational domain, the second goal is to visualize the additional data, i.e. 3D velocity field and electric current paths, which are not accessible to measurements in the experiment. Before we explain why one can successfully compute the experimental flow under and near the magnet using laminar calcu-

lations let us shortly describe in the next paragraphs the state of the art of numerical and theoretical approaches that could be appropriate to describe the present problem involving turbulence and inhomogeneous magnetic field at the same time.

The most ideal approach from the point of view of physical exactness would be to carry out a direct numerical simulation (DNS) of the experimental flow which models correctly the whole flow including turbulent regions down to small scales. However, to do this under a magnetic field steeply varying with space coordinates is extremely hard since it requires space and time resolution a few orders of magnitude more than is available today. Actually, to catch all spatial structures of the flow, especially Hartmann layers and sidewall jets, the simulation has to be fully three-dimensional and needs high resolution near the boundaries. This concerns also the turbulent flow which was generated in the experiment by a honeycomb at the inflow in order to observe suppression of fluctuations by the static magnetic field. The inflow distance takes almost half the length of the computational domain, therefore half of the computational resources must be paid to simulate correctly the flow without explicit action of the magnetic field, just to monitor declining turbulent fluctuations.

Other numerical approaches to catch turbulent features of the flow are Large eddy simulations (LES) and Reynolds averaged stress models (RANS). These are as well faced with serious technical difficulties. The present state of the art for LES of conducting fluids under magnetic fields is such that one may treat the flow inside a homogeneous magnetic field only if one resolves the boundary layers as in a direct numerical simulation (DNS), see [Knaepen and Moin (2004); Vorobev, Zikanov, Davidson, and Knaepen (2005)]. The definition of appropriate wall functions for the turbulent Hartmann and sidewall layers is still an actual field of research. LES in inhomogeneous magnetic field meets serious difficulties as one has to find appropriate methods of spatial averaging. For the momentary available RANS models it is not yet clear whether they are able to describe the unavoidable anisotropy of the turbulent scales inside strongly varying magnetic field, see [Widlund, Zahrai, and Bark (1998); Kenjerec and Hanjalic (2000, 2004)]. In any case, before to start a LES or RANS study one first has to define and verify parameters appearing in these phenomenological

models by DNS runs.

The usual analytical means also fail to describe the features of the experimental flow. This holds, because the parameters of the applied magnetic field lie outside the limits imposed by the assumptions necessary for any analytical theoretical treatment. In particular, to neglect inertial effects, the existing analytical approaches assume very strong and slowly varying magnetic field, which is not fulfilled neither for the electromagnetic brake nor for the channel flow considered here. Typically, any regular theoretical method is based on an asymptotic expansion of MHD equations around large N [see for example Lavrentiev, Molokov, Sidorenkov, and Shishko (1990) and references therein]. However, in the system under consideration, the local interaction number $N(x) = B_z(x)N$ goes up from zero to moderately high values on a short distance under the inward gradient of the magnetic field. Moreover, even if such an approach is not entirely impossible for some cases, it employs a series expansion what is of the same cost approximately as a full 3D simulation [Sellers and Walker (1999)]. Also, the theoretical methods do not take a span-wise dependence of the magnetic field into account, however, as we shall see later, this seemingly fine detail of the magnetic field configuration can be responsible for significant qualitative features in the electric potential distribution inside the magnetic gap.

However, as follows from the experimental data [Andreev, Kolesnikov, and Thess (2006)], the intensity of turbulent fluctuations inside the magnetic gap is lower than one percent, and essentially smaller than at the inlet distance at front of the magnetic system. This provides evidence that the magnetic field is strong enough to be the main influence shaping the flow structure inside the magnetic gap. This flow structure, qualitatively characterized by a M-shaped profile, is weakly dependent on the separate Re and Ha numbers and strongly dependent on the interaction parameter N , especially when N is high. Another conjecture from these experimental data is that the originally turbulent inlet velocity profile is of small importance as well.

The foregoing statements give us an opportunity to reproduce the experimental results using a laminar numerical 3D simulation. That means, we do not carry out a computation with the same values of Re and Ha as in the experiment and do not monitor turbulence. Instead, since the main effects are due to the interaction number N , one

may select for the simulation Re and Ha lower than in the experiment but belonging to the same ratio $N = Ha^2/Re$. As inlet flow one takes a laminar duct flow. To clarify, whether the shape of inflow velocity plays a role for the measured experimental data, one can test different laminar inflow profiles having the same mean flow rate but different flatness.

It is easy to point out a reasonable range for the Re numbers in the numerical simulation. Large Re parameter provokes turbulence which could not be properly resolved with current computational resources while too low Re number results in a viscous force in the core of the flow. On the other hand, the highest limit of the Re number is governed also by the value of Ha number which is, in its own turn, dictated by the available grid resolution for the Hartmann layer.

Thus, the main goals of the simulation were to determine the qualitative global velocity field and to find a good reproduction of the electric potential in the magnetic field region. Especially, we were interested to find the two extrema of the electric potential which were observed in the experiment. As it turns out, all these aims were reachable. The overall general features of the laminar flow are well represented by our code. In section 4.1 we present how the Hartmann layer and the sidewall jets are forming under the magnet in a stationary flow. For the electric potential under the magnet the experimental results of [Andreev, Kolesnikov, and Thess (2006)] show clearly (section 4.2) that the flow under the magnet is near to being laminar. In this region the magnetic and the inertial forces are predominant, if one excludes the regions very near to the walls where the viscous forces are essential. Therefore we find a good representation of the electric potential distribution of the experiment for our runs using lower Hartmann and Reynolds numbers but keeping the same interaction parameter.

The structure of the present paper is the following. In section 2 the equations and our numerical method to solve them are presented. Here also the inflow profiles and the used grid are specified. In section 3 some properties of the experimental magnetic field are explained and a second simplified magnetic field with no span-wise dependence is introduced, which serves to show that small changes on the inhomogeneous magnetic field can lead to remarkable differences in the electric potential distribution. In section 4 we present the results of our numerical computations showing all characteristics of the velocity

field (section 4.1), the comparison of the numerically determined electric potential with experimental data (section 4.2), and the electric current paths (section 4.3).

2 Equations and numerical method

The governing equations for electrically conducting and incompressible fluid are derived from the Navier-Stokes equation coupled with the Maxwell equations for moving medium, and also using the Ohm's law. We apply the quasi-static (induction-less) approximation where it is assumed that an induced magnetic field is infinitely small in comparison to the external magnetic field (see, e.g. [Roberts (1967)]), so it is neglected when one calculates the Lorentz force, but it is not neglected at finding the electric current density \mathbf{j} . The resulting equations in dimensionless form are then given as follows:

$$\frac{\partial \mathbf{u}}{\partial t} + (\mathbf{u} \cdot \nabla) \mathbf{u} = -\nabla p + \frac{1}{Re} \Delta \mathbf{u} + N(\mathbf{j} \times \mathbf{B}), \quad (1)$$

$$\nabla \cdot \mathbf{u} = 0, \quad (2)$$

$$\mathbf{j} = -\nabla \phi + \mathbf{u} \times \mathbf{B}, \quad (3)$$

$$\Delta \phi = \nabla \cdot (\mathbf{u} \times \mathbf{B}). \quad (4)$$

Here \mathbf{u} denotes velocity field, \mathbf{B} is an external magnetic field, \mathbf{j} is electric current density, p is pressure, ϕ is electric potential, $Re = u_0 H / \nu$ is Reynolds number, $N = Ha^2 / Re$ is the interaction parameter (Stuart number), and $Ha = HB_0(\sigma/\mu)^{1/2}$ is Hartmann number, all defined with the half-height of the channel H , mean velocity u_0 , typical magnetic field strength B_0 , density ρ , electric conductivity σ , kinematic ν and dynamic $\mu = \rho\nu$ viscosities.

As follows from eq. (1) the viscous force $\Delta \mathbf{u}$ is scaled by Reynolds number Re , therefore at high Re and far from the walls it plays a minor role. As a result the flow is governed by the interaction parameter N defining the ratio between magnetic and inertial forces. This is a case we treat in the paper under consideration by comparing experimental and simulated results with similar N and different (and high) Re numbers.

In the experiments [Andreev, Kolesnikov, and Thess (2006)], the eutectic alloy $\text{Ga}_{0.68}\text{In}_{0.20}\text{Sn}_{0.12}$ was used as a liquid metal. It has density $\rho = 6360 \text{ kg/m}^3$, electric conductivity $\sigma = 3.46 \cdot 10^6 \text{ Ohm}^{-1}$ and kinematic viscosity $\nu = 3.4 \cdot 10^{-7} \text{ m}^2/\text{s}$. Thus, the Hartmann number $Ha = HB_0(\sigma/\rho\nu)^{1/2}$ defined with half-height of the channel ($H = 1 \text{ cm}$) and magnetic field intensity

$B_0 = 0.504 \text{ T}$ is $Ha = 193$. The interaction parameter $N = Ha^2/Re$ was varied in the experiments by means of the mean velocity rate u_0 entering the Reynolds number $Re = Hu_0/\nu$. We have implemented the experimental range of interaction parameters by varying mainly Ha (up to 120) and keeping $Re = 400$, thus in the simulation $4 \leq N \leq 36$.

Unknowns of the equations (1 – 4) are the velocity vector field $\mathbf{u}(x,y,z)$, and two scalar fields: pressure $p(x,y,z)$ and electric potential $\phi(x,y,z)$. The domain of the flow is given by a rectangular channel (Fig. 1) ($|x| \leq L_x$, $|y| \leq L_y$, and $|z| \leq L_z$ with $L_x = 25$, $L_y = 5$, and $L_z = H = 1$) having the same aspect ratios (Length:Width:Height=25:5:1) as the experimental channel of [Andreev, Kolesnikov, and Thess (2006)]. (In this experimental paper, $H = 2$ is defined as a whole height of the channel, and in the present paper we take $H = 1$ as a half-height. Thus, the Re and Ha numbers given in [Andreev, Kolesnikov, and Thess (2006)] were divided by factor two here.) For the external magnetic field we used the magnetic field which was measured in the experiment and a second configuration, which is used for comparison (see section 3). The Hartmann number is based on the B_0 value in the center of the magnetic gap $x = 0, y = 0, z = 0$. Note, this B_0 value is not the maximal one, to fulfill curl- and divergence free requirements, the field is slightly increasing by approaching top and bottom walls at fixed $x = 0$ and $y = 0$.

To solve the partial differential equations (1 – 4) initial and boundary conditions have to be provided. Since we are interested in a stationary solution the initial conditions play no role (except for the speed of convergence), and for the boundary conditions we suppose a duct with electrically insulating and "no-slip" walls on the sides, top and bottom. Insulating and "no-slip" conditions require at the boundary Γ to impose that $u|_{\Gamma} = 0$, $\partial\phi/\partial\mathbf{n}|_{\Gamma} = 0$, where \mathbf{n} is normal vector to Γ . The outlet was treated as a force free (straight-out) border for the velocity. The electric potential at inlet and outlet borders was taken equal zero because the inlet and outlet are sufficiently far from the region of magnetic field.

For the inlet profile we made use of two possibilities. A self-consistent choice for laminar flow is the stationary laminar profile of an infinite rectangular duct known analytically in the form of a series expansion. In the experimental channel, however, the inflow is generated by a honeycomb shaping a more flat inflow profile in span-

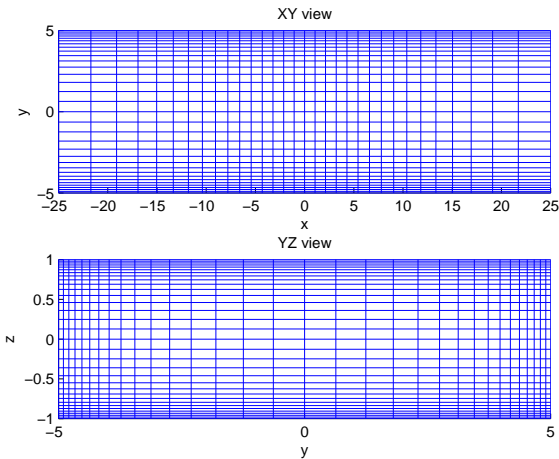


Figure 2: XY and YZ projections of the grid for the partition $N_x \times N_y \times N_z = 32 \times 32 \times 32$ and $R = 1.25$, $S = 0.75$, $T = 0.75$.

wise and vertical direction and generating vortex structures which give rise to decaying turbulence on the way of the liquid metal to the magnet. To study the influence of a more flat turbulent like profile on the electric potential under the magnet, we have generated a second inlet profile in the following well defined way: periodic boundary conditions (outflow=inflow) were imposed in stream-wise direction and then turbulent runs for the Reynolds number of the experimental system were performed. Then, by a space averaging procedure we computed the turbulent mean inflow profile. In spite of this careful check of the influence of inlet boundary conditions, we have found no difference in the final results between the laminar and the more flat turbulent inflows, except for the transitional region before the magnet. This shows that the magnetic field is sufficiently strong to completely govern the hydrodynamics of the flow when the magnetic region is reached. It agrees also with the experimental observation about measured turbulent fluctuations essentially suppressed inside the magnetic gap.

As a base for our solver we used NaSt3DGP - the simulation code developed in [Griebel, Dornseifer, and Neunhoeffler (1995)]. Originally, this finite difference solver was designed for pure hydrodynamical problems. Therefore we had to extend it by the following features to be able to solve MHD problems: (1) using the Poisson solver also for the determination of the electric potential, and (2) including

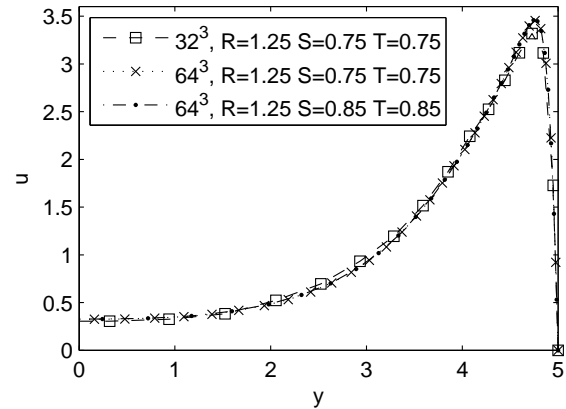


Figure 3: span-wise profile of the stream-wise velocity computed at different grid parameters: $N_x \times N_y \times N_z = 32 \times 32 \times 32$ (squares) and $64 \times 64 \times 64$ (crosses and dots), $(R, S, T) = (1.25, 0.75, 0.75)$ (squares and crosses) and $(1.25, 0.85, 0.85)$ (dots). Other parameters are common: $Re = 100$, $N = 16$, $x = 0$, $z = 0$.

the Lorentz force contribution on the right hand side computing the preliminary velocity field. Moreover, we reorganized the input and output parts of NaSt3DGP in order to work with the arrays keeping magnetic field, electric potential, and electric current.

Briefly, the numerical algorithm is the following. To decouple Eq. (1) - (4), the Chorin-type projection method is applied [Peyret and Taylor (1983); Hirsch (1988)]. This is a general procedure based on a predictor-corrector approach. First, the Poisson equation for the electric potential (4) is solved and the electric current is found according to (3). Next, a preliminary velocity field is computed from the momentum equation without regarding the influence of the pressure term. The second part of the time step from the preliminary velocity field, which is not divergence-free, to the new divergence-free velocity field allows to derive a Poisson equation for the new pressure. Thus, the whole algorithm is written down as follows (index n denotes time integration step, the spatial discretization is omitted):

1. Solve Poisson equation for the electric potential:

$$\Delta \phi^n = \nabla \cdot (\mathbf{u}^n \times \mathbf{B}).$$

2. Compute electric current:

$$\mathbf{j}^n = -\nabla \phi^n + \mathbf{u}^n \times \mathbf{B}.$$

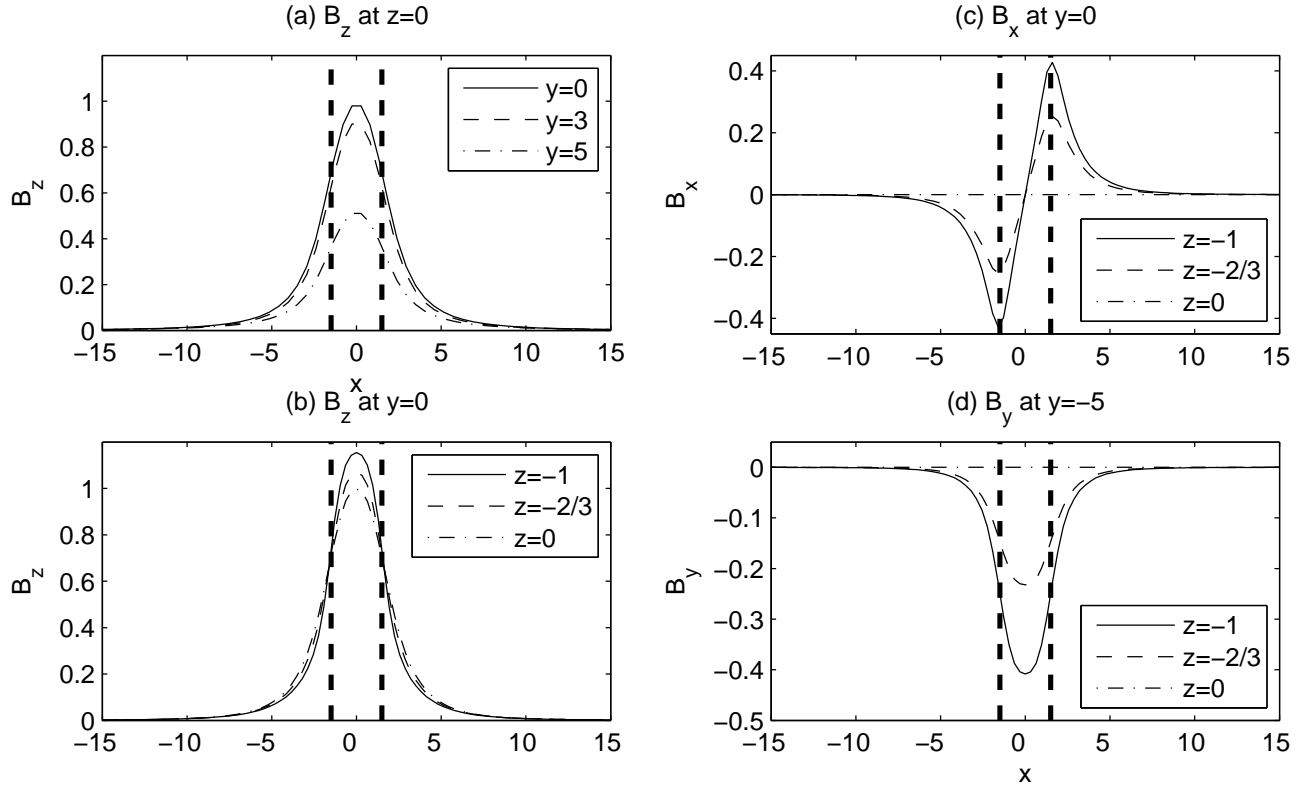


Figure 4: Cuts of the experimental magnetic field: transverse (plot *a* at $z = 0$ and plot *b* at $y = 0$), stream-wise (plot *c* at $y = 0$) and span-wise (plot *d* at $y = -5$) components. For plot *a*: $y = 0$ (solid), $y = 3$ (dashed), and $y = 5$ (dot-dashed); for plots *b* – *d*: $z = -1$ (solid), -0.66 (dashed), and 0 (dot-dashed). Plots *b* and *c* corresponds also to the simplified spanwise-homogeneous magnetic field discussed in the text. Bold dashed lines are the borders of the physical magnet.

3. With the known \mathbf{u}^n and \mathbf{j}^n , find the preliminary velocity field $\tilde{\mathbf{u}}$

$$\frac{\tilde{\mathbf{u}} - \mathbf{u}^n}{\delta t} = \frac{1}{Re} \Delta \mathbf{u}^n + N(\mathbf{j}^n \times \mathbf{B}) - (\mathbf{u}^n \cdot \nabla) \mathbf{u}^n.$$

4. To compute the velocity field \mathbf{u}^{n+1} of the next integration step one has to solve the Poisson equation for pressure

$$\Delta p^{n+1} = \frac{1}{\delta t} \nabla \cdot \tilde{\mathbf{u}},$$

and, as a result one finds

$$\mathbf{u}^{n+1} = \tilde{\mathbf{u}} - \delta t \nabla p^{n+1}.$$

The above algorithm is explicit and for simplicity it is presented as a scheme of first order precision. It describes the principal sequence, which in the code is realized with the Adams-Bashforth time step having second order precision. For pressure stabilization we apply

a staggered grid, and the VONOS (variable-order non-oscillatory scheme) scheme is used to discretize the convective and diffusive terms.

The solver is implemented to support parallel computation: the channel in the program code is subdivided into domains, and each domain is run as a separate process. Communication between the processes takes place at every integration step to synchronize the borders between the domains.

To make sure that all the layers are properly resolved in the simulation, we use an inhomogeneous 3D grid constructed in the following way. First, we map $-L_x \leq x \leq L_x$, $-L_y \leq y \leq L_y$, $-L_z \leq z \leq L_z$, onto three auxiliary variables $-1 \leq r \leq 1$, $-1 \leq s \leq 1$, $-1 \leq t \leq 1$ as follows:

$$r = \frac{th(R \frac{x}{L_x})}{th(R)}, \quad s = \frac{tg(S \frac{\pi y}{2L_y})}{tg(S\pi/2)}, \quad t = \frac{tg(T \frac{\pi z}{2L_z})}{tg(T\pi/2)},$$

and then variables r, s, t are uniformly partitioned into

N_x, N_y, N_z parts. There are three stretching parameters R, S, T providing a denser (R) grid at $x = 0$ and close to walls (S, T). Typical values used in the simulation are $R = 1.25$, and $0.75 \leq S \leq 0.95$, $0.75 \leq T \leq 0.95$. Fig. 2 gives an example of the grid for the partition $N_x \times N_y \times N_z = 32 \times 32 \times 32$ and $R = 1.25$, $S = 0.75$, $T = 0.75$. For each value of the Hartmann and Reynolds number in calculations, parameters R, S, T as well as the number of grid points were varied in order to obtain grid-independent results, see Fig. 3. The typical values used for the simulation were grid $64 \times 64 \times 64$ and $R = 1.25$, $S = 0.85$, $T = 0.85$.

3 Magnetic Field

The magnetic field used in the present paper was measured at equidistant points in the experiments [Andreev, Kolesnikov, and Thess (2006)], including all three components, and then interpolated on the grid points and stored into a three-dimensional array which is supplied as an input to the solver. This is the most general approach which enables us to work with any magnetic field configuration supplied externally. The details about the field are given in the experimental paper [Andreev, Kolesnikov, and Thess (2006)], here we just remind that it is created by means of two permanent magnets fixed outside on the top and bottom walls of the channel as is shown in Fig. 1. In the gap between the magnetic poles the field is aligned mainly along the vertical direction parallel to the z -axis. Outside of the gap, before and behind the poles, there are regions characterized by an inward and an outward gradient of the transverse magnetic field, see Fig. 4(a, b), where also the stream-wise component, B_x , plays a role (Fig. 4(c)). Since the physical magnets are finite in the span-wise direction (y -coordinate), the magnetic field is also dependent on the y coordinate, in particular, on the side walls a B_y component different from zero appears, Fig. 4(d). Moreover, the vertical component B_z is rather lower near the side walls ($y = \pm L_y$) in relation to B_z in the center ($y = 0$) (Fig. 4(a)). A few distinguished cross-sections of transverse, stream-wise, and span-wise magnetic field components along the x -axis are shown in Fig. 4. Other detailed plots of the magnetic field can be found in the experimental paper [Andreev, Kolesnikov, and Thess (2006)].

In addition to the experimental magnetic field configuration, which changes slightly along the y -axis, a few variants were simulated for a simplified magnetic field (in

the following always referred to as 'simplified magnetic field' in contrast to the 'experimental magnetic field') being independent of the y coordinate. The span-wise homogeneous field in this case originates from external magnets which are infinitely long in y -direction. It is characterized only by stream-wise $B_x(x, z)$ and transverse $B_z(x, z)$ components which coincide with $B_x(x, y, z)|_{y=0}$ and $B_z(x, y, z)|_{y=0}$ in the vertical slice ($y = 0$) shown in Fig. 4(b, c). It turns out that the span-wise decline of B_z near the side walls as well as that of the other \mathbf{B} components is of decisive influence on both the electric potential distribution and electric currents under the magnetic poles (see discussion in sections 4.2 and 4.3). This illustrates an importance of fine details of the localized heterogeneous magnetic field, which are usually neglected in theoretical computations.

4 Results of the simulation

This section is divided in three subsections focusing on different physical quantities — the velocity field, the electric potential, and the vector field of the current density — giving together an overview of the general and specific features of the experimental system. The known general features are the formation of a Hartmann profile in the transverse direction and the formation of an M-shaped profile in span-wise direction as well in the region of increasing and in the region of decreasing magnetic field (counted in stream-wise direction). In the first subsection we demonstrate that these two processes lead to a complex three-dimensional flow structure, which in the given magnetic field and channel proportions only can be determined numerically. For the electric potential distribution a direct comparison with experimental data is presented in the second subsection. A special feature showing up is a pair of extrema of the electric potential under the magnet. These extrema disappear when either the interaction parameter N is too small or the simplified span-wise uniform magnetic field (at any value of N) is used. The same sensible dependence of phenomena on the magnetic field structure is found in the last subsection for complicated helical current paths, which are present for the experimental magnetic field and are absent for the simplified magnetic field.

4.1 3D velocity field

We start from the well known phenomenon for duct flow under a locally heterogeneous magnetic field: the M-

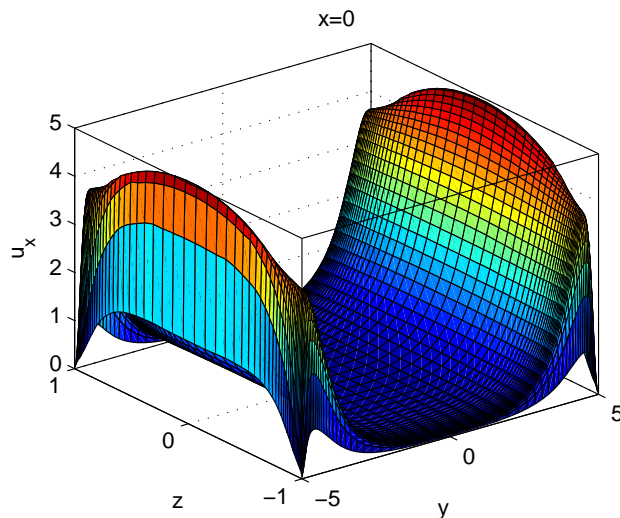


Figure 5: 3D M-shaped velocity profile, $x = 0$, $Re = 400$, $N = 36$

shaped velocity profile. It is shown in Fig. 5 for $Re = 400$ $N = 36$ at $x = 0$. Such a profile is a consequence of the braking effect of the magnetic field applied to the electrically conducting and moving fluid. Shortly, the effect can be understood in the following way: under the action of the externally applied magnetic field, electric currents are induced in span-wise direction. The larger the intensity of the magnetic field \mathbf{B} , the higher the density of the electric current \mathbf{j} . The channel walls are insulating and the magnetic field is locally heterogenous, therefore, to make a closure the electric currents will leave the area of the high magnetic field (see also the figures in section 4.3). Then, as \mathbf{j} and \mathbf{B} are both present, the Lorentz force $\mathbf{F}_L = \mathbf{j} \times \mathbf{B}$, hampers stream-wise fluid movement in the bulk of the channel. The flow tries to circumvent the area of high magnetic field as much as possible, and, as a result, the stream-wise velocity profile will adopt M-shaped in span-wise direction, and a stagnant region with stream-wise velocity about zero (see solid lines in Fig. 6) forms inside the magnetic gap. Various M-shaped surfaces are given in [Sterl (1990)], including their discussion and corresponding references. It is worth to note that the external magnetic field selected in [Sterl (1990)] for the simulation was either divergence- or curl-free, but not simultaneously divergence- and curl-free, nevertheless this did not disturb the formation of a M-shaped profile.

Fig. 6 shows the influence of the interaction parameter

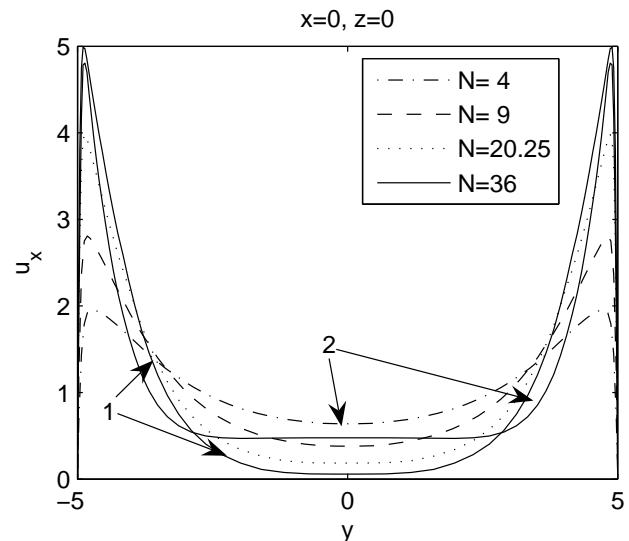


Figure 6: Stream-wise velocity profiles in span-wise direction in the center of the magnetic gap ($x = 0$ and $z = 0$), $Re = 400$ and $N = 4$ (dot-dashed), $N = 9$ (dashed), $N = 20.25$ (dotted), $N = 36$, experimental field (solid line 1) and $N = 36$, simplified field (solid line 2).

N on the M-shaped velocity profile. The effect is clear: the higher the value of N the stronger the Lorentz force braking the flow, the lower the velocity in the center, and thus the more pronounced the stagnant region. The solid curves 1 and 2 in Fig. 6 are related to the same parameter values $Re = 400$, $N = 36$, but to different magnetic fields: the experimental field (curve 1) and the simplified field (curve 2). This comparison shows that the character of the flow in this two cases is rather different. In particular, for the case of simplified field, the width of the stagnant region is larger but its level is higher than in the case of the experimental field. This can be explained by the decrease of B_z in span-wise direction for the experimental magnetic field. As the transverse magnetic field near the side walls consequently for the experimental field is lower than in the center, the liquid can more easily flow around the "magnetic obstacle" (see below), therefore the redistribution of the flow for the experimental magnetic field is more pronounced than for the simplified field.

Fig. 7.

Another insight for the M-shaped profile formation might be taken from the XY vector velocity plot shown in It was noticed several times a kind of similarity between the flow of an electrically conducting liquid pass-

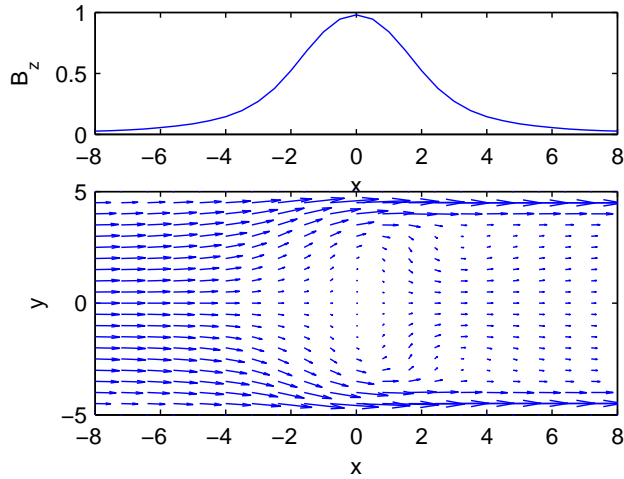


Figure 7: Vector plot of the velocity field in the central horizontal plane, $z = 0$. The upper part shows the intensity of the magnetic field on the straight line $z = 0$, $y = 0$, $Re = 400$, $N = 36$.

ing through an area of high local heterogeneous magnetic field (magnetic obstacle) and the well known flow around a bluff body (see e.g. [Cuevas, Smolentsev, and Abdou (2006)]). One can see that the velocity vectors envelop the central part of the channel nearly in the same way as it would be for a solid cylindrical obstacle in a two-dimensional flow. The only difference is that a real body creates a region with no fluid, say velocity zero, while in the region with magnetic field there still is fluid, but with very small velocity.

To analyze span-wise and vertical velocity components we have plotted a series of vector plots in vertical sections of the channel at several fixed values of x . They are shown in Fig. 8 to highlight the intrinsic three-dimensional nature of the velocity field. In the region of increasing magnetic field before the magnet gap (see Fig. 8a), the velocity vector in the vertical section is nearly aligned towards the corners of the channel. This can be explained by the simultaneous action of two effects: (i) the beginning tendency to form a M-shaped profile, and (ii) the formation of Hartmann layers which is accompanied by a flattening of the velocity profile in vertical direction (see also Fig. 9 below). The second reorganization process of the flow is accomplished faster, i.e. finished already at smaller x -coordinate, than the first one. This can be concluded from the second sec-

tion, Fig. 8b, because the plotted vectors indicate only a movement in the span-wise direction.

The formation of M-shaped profile continues further when the flow passes the maximum of the magnetic field, see Fig. 8c. However, as the flow reaches the region of decreasing magnetic field, there is an inversion of the span-wise movement (Fig. 8d): now it is opposite to the one observed before the magnet. These two processes — flow towards the side walls at the front of the magnetic gap and towards the center (i.e., away from the side walls) after the gap — demonstrate again that the flow passing a heterogeneous magnetic field has an analogy with the flow around an obstacle. Increasing further the x -value of the vertical section and thus leaving the region with noticeable magnetic field, the Hartmann profile begins to transform back into a parabolic profile. Consequently, there must be a *vertical* movement from the bottom and top walls towards the center, see Fig. 8e (note: we are only speaking about the vertical velocity component; the span-wise velocity component in section e is directed away from the center, compare with Fig. 7). This phenomenon is opposite to that observed in Fig. 8a: now there is no more braking force keeping the velocity profile flattened in the vertical direction. As a result, the flow develops a swirling component in the channel corners. The swirling behavior extends far behind the magnet, see Fig. 8f. To our knowledge, this effect of swirling flow in the corners inside the rectangular channel after passing the region of heterogeneous magnetic field has not been mentioned before elsewhere.

To get more insight how the vertical velocity redistribution takes place, Fig. 9 presents a vertical section along the midplane in stream-wise direction of the channel. The velocity vectors shown are the projection (u_x, u_z) of the total velocity. One clearly sees how the vertical velocity profile flattens before the magnet and becomes more convex after the magnet. Interestingly, the flattening starts in the center of the profile because of the action of the Lorentz force while the decay of the Hartmann layers begins at the top and the bottom wall because of the wall friction and viscosity in the fluid. The isolines of the normalized vertical profile $p(z;x)$ in Fig. 9 give an additional information to judge how flat the profile is at a given stream-wise coordinate x . We define the normalized vertical profile as $p(z;x) = u_x(x,0,z)/u_0(x)$, where $u_0(x) = \frac{1}{2} \int_{-1}^1 u_x(x,0,z) dz$ is the mean velocity in the vertical middle plane at given x and $y = 0$. Horizontal iso-

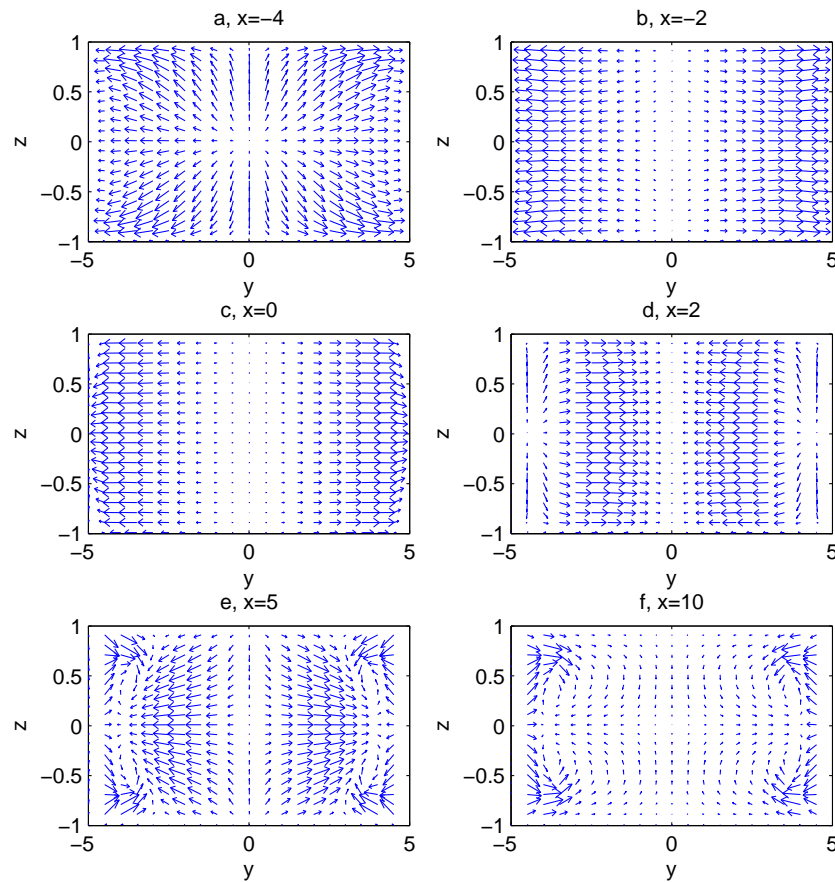


Figure 8: Vector plots of the vertical and span-wise velocity components at the following vertical sections of the channel: (a) $x = -4$, (b) $x = -2$, (c) $x = 0$, (d) $x = 2$, (e) $x = 6$, (f) $x = 11$ at $Re = 400$, $N = 36$. An interesting feature is the swirling flow that arises in the corners behind the magnet (plot e, f).

lines in Fig. 9 correspond to a profile, where the velocity changes in the vertical direction as for the parabolic profile in the inflow region, while the almost vertical isolines under the magnet represent regions with a flat profile, i.e. the Hartmann profile. Before (behind) the magnet the isolines converge (diverge) which demonstrates again the flattening (de-flattening) of the vertical velocity profile. The flattening process turns out to take place much faster (in four length units) than the de-flattening which is far from being finished in the six shown length units after the magnetic gap.

4.2 Electric potential

One main focus of this work is the demonstration that the flow under the magnet is determined by the value of the

interaction parameter N , independently of the individual values of the Hartmann and Reynolds numbers as long as the Reynolds number is high enough. For this aim we first start with a comparison of two numerical computations for the same interaction number N but with different Reynolds numbers. Fig. 10 shows such a comparison at $N = 16$ for $Re = 900$ (solid lines) and $Re = 225$ (dashed lines). One can actually see that the two contour line sets are not prominently distinct despite the fact that for both cases the Re numbers differ by a factor of 4, and the Ha numbers differ by a factor of 2. Before the magnetic gap the dashed and solid lines closely coincide with each other, and after the magnets there is a slight discrepancy since the inertial force for $Re = 900$ is higher than for $Re = 225$. More discrepancies one can find in the thick-

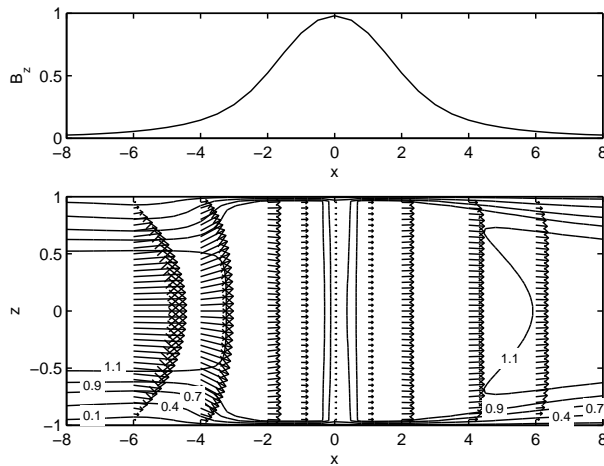


Figure 9: Vector plot of the velocity components u_x and u_z in the central vertical plane at $y = 0$, $Re = 400$, $N = 36$. The isolines are plotted at constant level of the normalized vertical profile $p(z;x)$ and give additional information about the flatness of the velocity profile.

nesses of viscous boundary layers, however they are essentially of no importance since we are interested in the processes taking place in the central part of the magnetic gap.

Now let us explain qualitatively the electric field distribution in the system under consideration. In the quasi-static approximation the current according to Ohm's law eq. (3) is the sum of two terms: the electric field induced by the motion of the conducting fluid volume inside the magnetic field, $\mathbf{u} \times \mathbf{B}$, and the electric field $\mathbf{E} = -\nabla\phi$ derived from an electric potential ϕ generated inside the fluid volume because of the solenoidality of the electric current (due to Ampère's law $\nabla \times \mathbf{B} = \mu\mathbf{j}$) and the isolating boundary conditions at the walls forcing currents to close inside the fluid volume. Taking the divergence of (3) one gets the Poisson equation (4) for which the right hand side $\nabla \cdot (\mathbf{u} \times \mathbf{B}) = \mathbf{B} \cdot \mathbf{w}$ plays the role of the inhomogeneity². Comparing with the Poisson equation for usual electrodynamics, $\Delta\phi(\mathbf{r}) = -\rho(\mathbf{r})/(\epsilon_0\epsilon)$, one sees that the expression $\rho^* = -\epsilon_0\epsilon\mathbf{B} \cdot \mathbf{w}$ can be considered formally as an electric charge density induced by the movement of the electrically conducting fluid in the magnetic field. In

²The second term $\mathbf{u} \cdot (\nabla \times \mathbf{B})$ vanishes because the fluid volume is outside of the external magnet and induced magnetic fields are neglected in the quasi-static approximation.

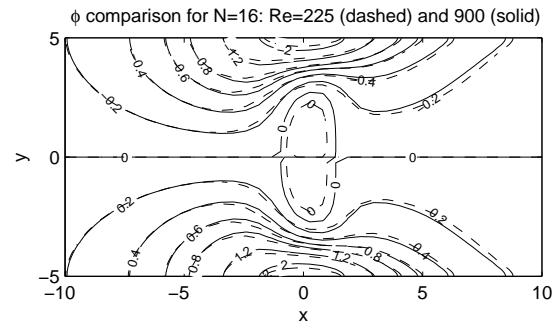


Figure 10: Electric potential distribution, $\phi(x,y)$ in central horizontal plane ($z = 0$) for $N = 16$, simulation: $Re = 900$ (solid) and $Re = 225$ (dashed).

the duct flow, the largest contributions to $\mathbf{B} \cdot \mathbf{w}$ are generated with the predominant vertical component B_z of the magnetic field together with the span-wise velocity gradient $\partial u_x / \partial y$ of the stream-wise velocity component, i.e. $\rho^* \approx \epsilon_0\epsilon B_z (\partial u_x / \partial y)$. Therefore, looking in stream-wise direction, one finds a negative charge density near the left wall and a positive charge density near the right wall of the channel which correspond to the outer flanks of the M shape profile under the magnet. The electric field created by this charge density inside of the channel points in span-wise direction *parallel* to the y axis³. (The y axis points from the right to the left wall of the channel). The braking action of the Lorentz force leads to a strongly diminished flow in the central region under the magnet and in this way the M shape profile is created. The inner flanks of the M shape profile provide opposite velocity gradients and opposite charge densities causing an electric field *antiparallel* to the y -axis in the central region. It depends now on the strength of the magnetic field and the corresponding braking effect, whether there exists a region in the middle of the channel under the magnet, where the total electric field — the sum of both described charge densities from the outer and inner flank of the M shape profile — is antiparallel. In this case the electric field has to change its sign two times along the span-wise direction, corresponding to three sign changes for the electric potential. In the contour plot of the electric potential, the stagnant region is manifested by closed

³Two remarks: (1) The electric field direction coincides, of course, with the direction of $\mathbf{u} \times \mathbf{B}$. (2) Directly at the walls the charge density is high, but the induced electric field has to be zero because of the isolating boundary condition.

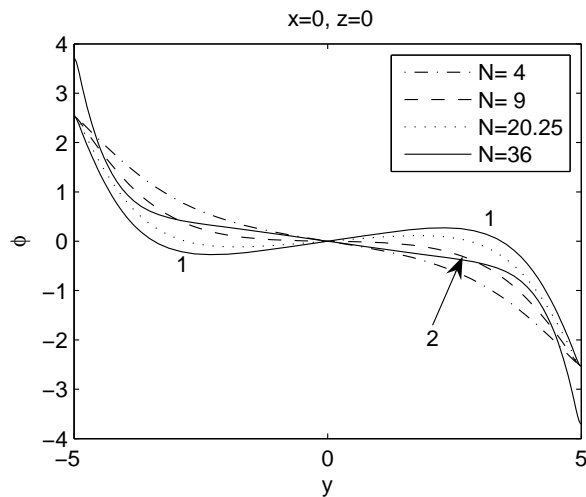


Figure 11: Simulated span-wise electric potential profiles in the center of the magnetic gap ($x = 0$ and $z = 0$), $Re = 400$ and $N = 4$ (dot-dashed), $N = 9$ (dashed), $N = 20.25$ (dotted), $N = 36$, experimental magnetic field (solid line 1) and $N = 36$, simplified field (solid line 2).

contour lines as we shall see below in Fig. 13, 14.

To illustrate the previous deduction about electric potential behavior we plotted in Fig. 11 span-wise profiles of ϕ for different interaction parameter N . One can see that for the low interaction parameter $N = 4$ (dot-dashed) $\phi(y)$ shows clearly monotonic behavior, while for the high interaction parameter $N = 36$ (solid line 1) the sign of the electric potential changes three times. Corresponding curves in Fig. 6 and 11 are plotted with the same line types. One clearly observes the tendency: the development of the inflection of the $\phi(y)$ curves (Fig. 11) is accompanied by a lower minimum of the velocity profile (Fig. 6) around $y = 0$.

The next two figures show how the electric potential changes by passing the magnetic field region. They are given in comparison with the experimental results. Fig. 12(a) shows the profiles for $N \approx 20$ and Fig. 12(b) shows the profiles for $N \approx 9$. As it should be, kinks of the electric potential in Fig. 12(a) are more expressive than in Fig. 12(b) due to the larger interaction parameter. Also, the figures demonstrate that this effect is most expressive in the center of the magnetic gap ($x = 0$) where the magnetic field and, therefore, the braking Lorentz force is maximal. In the region of the inward ($x = -2$) and outward ($x = 2$) magnetic field gradient, electric poten-

tial behavior is monotonic. The comparison between the simulated and experimental results reveals almost perfect accordance.

To complete the comparison with the experimental [Andreev, Kolesnikov, and Thess (2006)] data we present also the contour plots. Fig. 13 shows the experimental and numerical results of the electric potential distribution at $N \approx 20$. Two contour plots give the level lines of the electric potential, the first, as it was directly and systematically measured in the experiment, and the second, as computed numerically. Qualitatively, the electric potential distribution has the following main features: (i) it is an antisymmetric AI contour map with respect to the axis $y = 0$ (ii) there are two global extrema directly at the side walls exactly under the peak of the magnetic field ($x = 0$) and (iii) there are two local sign alternating extrema slightly shifted in stream-wise direction at one third distance from the side wall (measured by the total span-wise width of the channel), Fig. 13. As one can see, all the features of the experimental electric potential measured at $Re = 2000$ are excellently reflected in the simulation at $Re = 400$ since both have the similar interaction parameter, $N \approx 20$. Another comparison for $N \approx 9$ is given in Fig. 14. Now, the closed lines of the electric potential are weaker because of the lower interaction parameter. The good accordance between experimental and simulated results is observed in Fig. 14 as well.

Summing up, we find a very good agreement between the experimental and the numerical results comparing data for the same interaction parameter N . This holds even in complementary regimes with respect to the Reynolds number: turbulent inflow in the experiment, and laminar calculations in the simulation. This shows that the interaction parameter indeed is the governing parameter for the flow under and near to the magnets, and that the flow in this region is determined by the magnetic and inertia forces. If the Reynolds number is not high enough, the viscous force begins to play a role as a third force in the system as can be observed to a small extent in our first comparison, see Fig. 10, of this subsection.

As the electric potential does not show a visible reaction on turbulence or no turbulence in the inflow, one could conclude that it is a quantity which is rather insensitive to different influences. We will show now that this is not the case, and consider for this aim the action of the span-wise decrease of the experimental magnetic field on the electric potential distribution. This dependence is

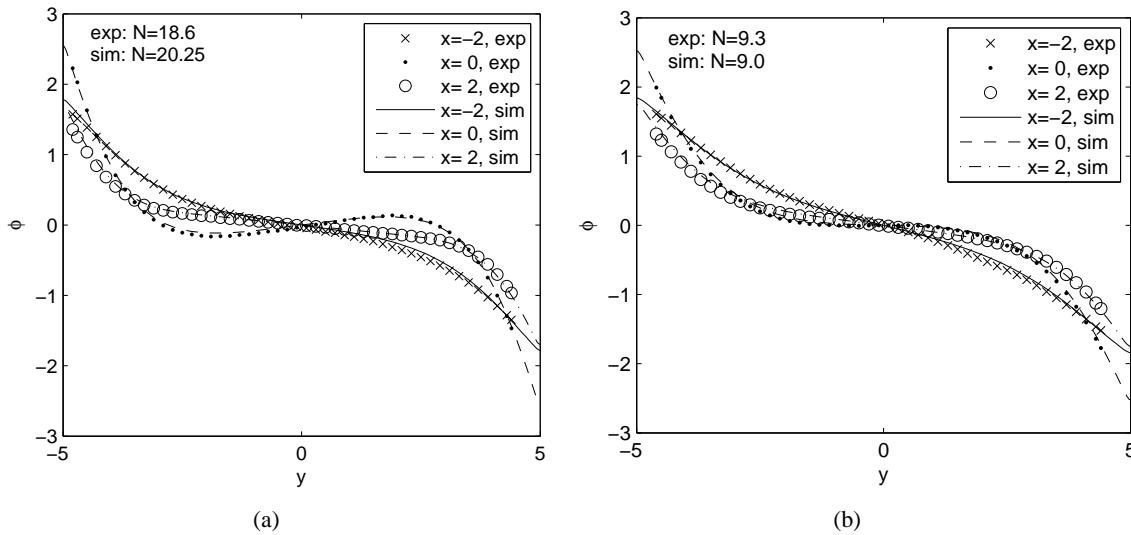


Figure 12: Experimental (symbols) and simulated (lines) span-wise electric potential profiles at $z = 0$ and $x = -2$ (crosses and solid lines), 0 (dots and dashed lines), 2 (circles and dot-dashed lines). Plot *a* is for $N \approx 20$: $(Re, N) = (2000, 18.6)$ (experiment) and $(Re, N) = (400, 20.25)$ (simulation). Plot *b* is for $N \approx 9$: $(Re, N) = (4000, 9.3)$ (experiment) and $(Re, N) = (400, 9)$ (simulation).

especially interesting, since many people believe that in most cases only the transverse component of the magnetic field, changing along stream-wise coordinate, is of importance. For instance, most of the numerical simulations were performed only with $B_z(x)$ dependence, see, e.g. [Sterl (1990); Alboussiere (2004)]. To clarify the role of the magnetic field and demonstrate the sensitivity of the $\phi(x, y)$ map, we fixed $(Re, N) = (400, 36)$ and compare two variants with the real experimental (showing y -dependence) and simplified (span-wise uniform) magnetic field. As it is supposed typically, the simplified magnetic field has only stream-wise dependence in its intensity, and is constant at every fixed x in span-wise direction. The simulated results for the simplified field are presented in Fig. 15. One discovers that now the picture changes even qualitatively: there are no more closed lines of the electric potential, that is, the potential drops monotonically from one side wall to another (compare also the solid curves 1 and 2 in Fig. 11). This is a strong indication that the factors, which are decisive for the comparison of experimental and simulated results, are the maximal interaction parameter in the magnetic gap and the proper configuration of the magnetic field.

4.3 Electric currents paths

Fig. 16 shows the closure of the electric currents in the central horizontal plane ($z = 0$) which were calculated as lines tangent at every point to the vector of electric current \mathbf{j} . For sake of simplicity only few paths are shown, one in the region of increasing magnetic field, and others after the magnet in the region of decreasing field. In the case of constant magnetic field the loops of the electric current are located entirely in vertical planes and most of the current is concentrated in the Hartmann layers. By contrast, in the case of the heterogenous magnetic field, since an electric current intends to close itself in the region where magnetic field is minimal (in order to close along paths with smallest resistance), one sees the current loops close themselves in the horizontal planes. The characteristic length of the loops is rather large as can be seen in Fig. 16: the turning point of \mathbf{j} , starting under the peak of the magnetic field ($x \approx 0$), is at $|x| \approx 10 \dots 15$, while a remarkable magnetic field intensity is felt only up to $x \approx 5$. This fact must be taken into consideration when one selects where to put inlet and outlet of the numerical simulation box, otherwise it is possible to get artificial findings.

Fig. 16 reveals small closed loops for the electric current at $x \approx 2.2$ and $y \approx \pm 4.1$. These loops are interesting be-

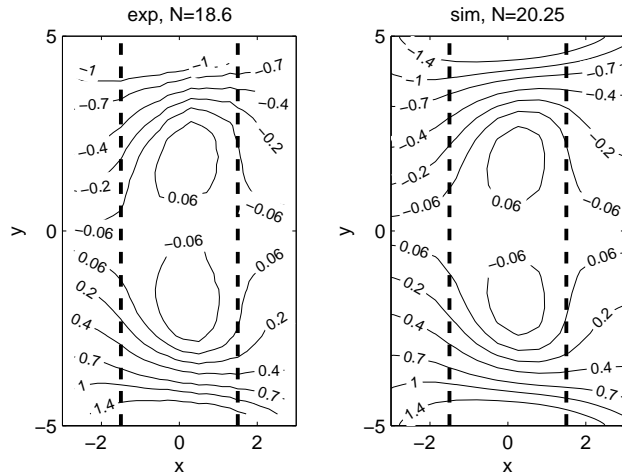


Figure 13: Electric potential distribution, $\phi(x,y)$, in the central horizontal plane ($z = 0$) for $N \approx 20$: experiment, $Re = 2000, N = 18.6$ (left) and simulation $Re = 400, N = 20.25$ (right). Bold dashed lines are physical borders of the magnetic gap.

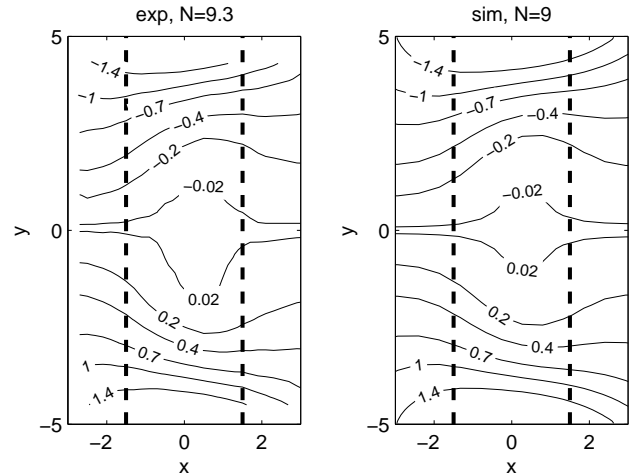


Figure 14: Electric potential distribution, $\phi(x,y)$ in central horizontal plane ($z = 0$) for $N \approx 9$: experiment, $Re = 4000, N = 9.3$ (left) and simulation $Re = 400, N = 9$ (right). Bold dashed lines are physical borders of the magnetic gap.

cause of the closure of the electric current is typically a big horizontal loop which envelops the space of the magnetic field gradient. The geometric explanation for these small exotic loops is that they are projections to the XY plane from complicated electric paths developing essentially in 3D space. Fig. 17 clearly shows these 3D paths: they are helices connecting the Hartmann layer and the middle horizontal plane.

As well in our calculation presented in this paper, see Fig. 17, as also in other calculations which are not shown here, helical current paths are only present when the level lines of the electric potential relief in the horizontal mid-plane contains closed lines, see Fig. 13. Our results strongly suggest that the presence of closed lines of the electric potential is a necessary condition for the appearance of helical current paths. As the span-wise uniform magnetic field does not lead to a triple change of the span-wise electric potential profile (i.e. no closed lines in Fig. 15), the 3D paths of the electric currents for this case consequently are simple closures in the horizontal plane as is shown in Fig. 18.

There are also correlations between the span-wise inhomogeneity of the magnetic field, 3D helical currents, and features of the stagnant region in M-shaped velocity profiles. One sees a broad constant plateau in $u_x(y)$ for the

simplified field while for the experimental field there is a degraded minimum approaching zero (compare solid curves 1 and 2 in Fig. 6). Since the level of the stagnant plateau for the span-wise uniform magnetic field is sufficiently high to keep electromotive contribution $\mathbf{u} \times \mathbf{B}$ in the electric current \mathbf{j} , there is no double sign change of the electric potential $\phi(y)$ (compare solid curves 1 and 2 in Fig. 11). The stagnant plateau is not so broad but considerably lower for the experimental magnetic field, because of the lower magnetic field strength near the side walls. The latter induces the braking Lorentz force near side walls to be smaller than in the center. As a result, the case of the real field looks somehow as a flow around the magnetic obstacle, while the simplified field is looks more similar to an uniform semi-penetrable barrier.

The 3D helices of the electric current in the case of the real field (Fig. 17) arise near the turning points where the electric field \mathbf{E} changes its sign, hence $E \sim 0$. These helices are maintained mainly by the electromotive component $(\mathbf{u} \times \mathbf{B})$ in Ohm's law, eq. 3. On the other hand, these helices are located in the region of space where stream-wise component $B_x(x)$ reaches the largest value, see Fig. 4, in the center of the outward magnetic field region. Referring to the vector product $\mathbf{u} \times \mathbf{B}$, we see that the term $u_y B_x$ is of importance for the size of the j_z component, which is responsible for the uprise of the helix.

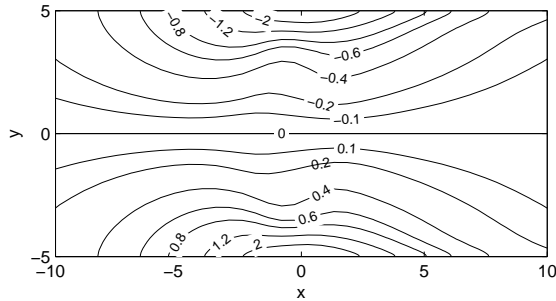


Figure 15: Electric potential distribution, $\phi(x, y)$ in central horizontal plane $z = 0$ for $Re = 400$, $N = 36$, and magnetic field without span-wise dependence.

Thus, in order to catch the helices one has to keep in the simulation all the components of the magnetic field.

5 Conclusions

We have carried out numerical simulations for liquid metal channel flow under inhomogeneous magnetic field. For the computations the same channel geometry and the magnetic field configuration as in the experiment of [Andreev, Kolesnikov, and Thess (2006)] were used.

Computations of the velocity field showed that all known general features — like for example the formation of Hartmann layers at the walls perpendicular to the main component of the magnetic field, or the formation of an M shaped profile in span-wise direction — are represented correctly by our numerical code. All features of the flow together lead to a complex three-dimensional flow structure, which for the investigated regime of interaction parameters, $4 \leq N \leq 36$, can only be determined numerically. As a new feature of the velocity field a swirling flow in the corners of the duct is observed. It begins shortly after the magnetic gap and extends far into the outflow region.

The main goal of this work was to compare the electric potential distribution measured in the experiment with that of our numerical simulation. We were able to find a very good agreement of the electric potential distribution for two sets of parameters which were used in the experiment ((i) $N = 18.6$, $Re = 2000$, and (ii) $N = 9.3$, $Re = 4000$) and the corresponding sets ((i) $N = 20.25$, $Re = 400$, and (ii) $N = 9$, $Re = 400$) in our numerical cal-

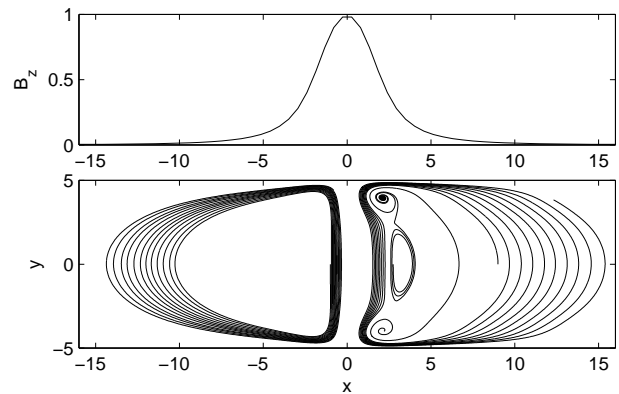


Figure 16: Electric current paths in the central horizontal plane ($z = 0$) under the experimental magnetic field, $Re = 400$, $N = 36$. The lines are not equidistant since they were obtained by integration from a few starting points at $(x, y) = (-0.5, 0), (0.5, 0), (2.1, 4.1), (2.1, -4.1)$.

culations. This comparison shows that the electric potential distribution in the magnetic field region is solely determined by the value of the interaction parameter. This makes sense as in the magnetic field region the Lorentz force and the inertial force are strongest, while the viscous force is only important in the Hartmann layers and near to the side walls. The turbulence, which is present in the inflow of the experimental channel is in the magnetic field region already negligible and has no influence on the electric potential distribution. A numerical test with a different inflow profile, which is more flat like a turbulent profile, also showed no difference.

In addition, we could demonstrate that local extrema of the electric potential appear for interaction parameter higher than a critical value, which lies between 9 and 18. Simulations with a simplified magnetic field (only dependent on vertical and stream-wise coordinate, no span-wise field component) showed that local extrema of the electric potential map totally vanish in this case. This means that already a slight variation of the inhomogeneous magnetic field can have a strong influence of the electric potential distribution. The same sensitivity on the magnetic field structure is found for the electric current density: In the case of the experimental magnetic field our computations revealed the appearance of com-

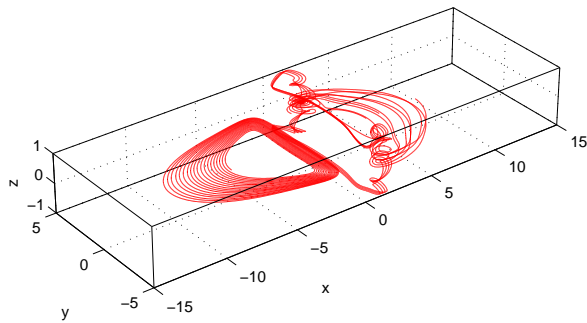


Figure 17: 3D electric current path for the experimental magnetic field.

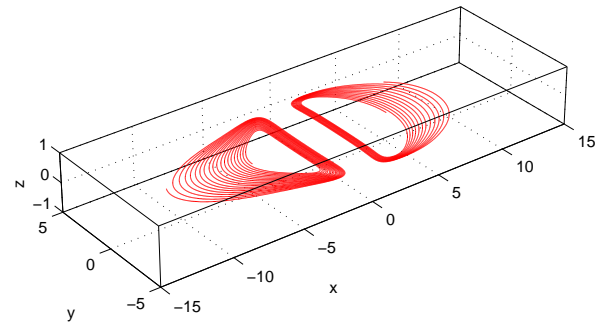


Figure 18: 3D electric current path for the simplified magnetic field without span-wise dependence.

plicated helical current lines which are not present for the simplified magnetic field.

Acknowledgement: The authors express their gratitude to the Deutsche Forschungsgemeinschaft for financial support in the frame of the "Research Group Magnetofluidynamics" at the Ilmenau University of Technology under grant ZI 667/2-3. The simulations were carried out on a JUMP supercomputer, access to which was provided by the John von Neumann Institute (NIC) at the Forschungszentrum Jülich. We are grateful for many fruitful discussions with Andre Thess. Special thanks go to our experimental colleagues, Yuri Kolesnikov and Oleg Andreev, for an always close exchange of thoughts and providing the experimental data to compare with our numerical results. As well, the authors appreciate the scientific exchange on our subject with Yves Delannoy and Jacqueline Etay in Grenoble, France, which was supported by the Deutscher Akademischer Austauschdienst.

References

Alboussiere, T. (2004): A geostrophic-like model for large Hartmann number flows. *J. Fluid Mech*, vol. 521, pp. 125–154.

Andreev, O.; Kolesnikov, Y.; Thess, A. (2006): Experimental study of liquid metal channel flow under the

influence of a non-uniform magnetic field. *Phys. Fluids*, vol. 18, pp. 065108.

Cuevas, S.; Smolentsev, S.; Abdou, M. (2006): On the flow past a magnetic obstacle. *JFM*, vol. 553, pp. 227 – 252.

Davidson, P. (1999): Magneto hydrodynamics in Materials Processing. *Annual Review of Fluid Mechanics*, vol. 31, pp. 273–300.

Griebel, M.; Dornseifer, T.; Neunhoffer, T. (1995): *Numerische Strömungssimulation in der Strömungsmechanik*. Vieweg Verlag, Braunschweig.

Hirsch, C. (1988): *Numerical computation of internal and external flows. Volume I and II*. John Wiley and Sons, Chichester.

Kenjerec, S.; Hanjalic, A. (2000): On the implementation of effects of Lorentz force in turbulence closure models. *Int. J. of Heat and Fluid Flow*, vol. 21, pp. 329–337.

Kenjerec, S.; Hanjalic, A. (2004): A direct-numerical-simulation-based second-moment closure for turbulent magnetohydrodynamic flows. *Physics of Fluids*, vol. 16, no. 5, pp. 1229–1241.

Knaepen, B.; Moin, P. (2004): Large-eddy simulation of conductive flows at low magnetic Reynolds number. *Physics of Fluids*, vol. 16, no. 5, pp. 1255–1261.

Lavrentiev, I.; Molokov, S.; Sidorenkov, S.; Shishko, A. (1990): Stokes flow in a rectangular magnetohydrodynamic channel with nonconducting walls within a nonuniform magnetic field at large Hartmann numbers. *Magnetohydrodynamics*, vol. 26, no. 3, pp. 328–338.

Peyret, R.; Taylor, T. (1983): *Computational methods for fluid flow*. Springer-Verlag, New York.

Roberts, P. H. (1967): *An introduction to Magnetohydrodynamics*. Longmans, Green, New York.

Sellers, C.; Walker, J. (1999): Liquid-metal flow in an electrically insulated rectangular duct with a non-uniform magnetic field. *Int. J. Eng. Sci.*, vol. 37, pp. 541–552.

Sommeria, J.; Moreau, R. (1982): Why, how, and when, MHD turbulence becomes two-dimensional. *J. Fluid Mech*, vol. 118, pp. 507–518.

Sterl, A. (1990): Numerical simulation of liquid-metal MHD flows in rectangular ducts. *J. Fluid Mech*, vol. 216, pp. 161–191.

Takeuchi, S.; Kubota, J.; Miki, Y.; Okuda, H.; Shiroyama, A. (2003): Change and trend of molten steel flow technology in a continuous casting mould by electromagnetic force. In *Proc. EPM-Conference*, Lyon, France.

Thess, A.; Votyakov, E.; Kolesnikov, Y. (2006): Lorentz Force Velocimetry. *Phys. Rev. Lett.*, vol. 96, pp. 164501.

Vorobev, A.; Zikanov, O.; Davidson, P.; Knaepen, B. (2005): Anisotropy of magnetohydrodynamic turbulence at low magnetic Reynolds number. *Physics of Fluids*, vol. 17, pp. 125105.

Widlund, O.; Zahrai, S.; Bark, F. (1998): Development of a Reynolds stress closure for modelling of homogeneous MHD turbulence. *Physics of Fluids*, vol. 10, pp. 1987.

